



The Solar Photospheric Continuum Brightness as a Function of Mean Magnetic Flux Density. I. The Role of the Magnetic Structure Size Distribution

C. L. Peck^{1,2,3} , M. P. Rast^{2,4} , S. Criscuoli³ , and M. Rempel⁵ 

¹Department of Physics, University of Colorado, Boulder, CO 80309, USA

²Laboratory for Atmospheric and Space Physics, Boulder, CO 80303, USA

³National Solar Observatory, Boulder, CO 80303, USA

⁴Department of Astrophysical and Planetary Sciences, University of Colorado, Boulder, CO 80309, USA

⁵High Altitude Observatory, National Center for Atmospheric Research, Boulder, CO 80307, USA

Received 2018 August 17; revised 2018 November 12; accepted 2018 November 19; published 2019 January 11

Abstract

Solar irradiance models indicate that irradiance variations are dominated by changes in the disk-coverage of magnetic structures, whose brightness is thought to be determined by their size and average magnetic flux density. Recent results suggest that the brightness of small-scale magnetic structures also depends on the mean magnetic flux of the extended region surrounding them due to reduced convective vigor. Low spatial resolution, however, may limit the ability to distinguish the role of magnetic structure size distributions from that of the mean magnetic flux. Using high-resolution 3D MHD simulations, we investigate the brightness of magnetic structures embedded in regions characterized by different mean magnetic flux. In agreement with previous results, we find reduced brightness with increasing mean magnetic flux when comparing the pixel-by-pixel continuum brightness versus magnetic field strength. Evaluating equivalently sized magnetic structures, however, we find no significant dependence of the magnetic structure brightness on the mean magnetic flux of the region in which they are embedded. Rather, we find that simulations with larger mean magnetic flux generate larger, and therefore darker, magnetic structures whose contributions result in an overall darkening of the region. The differences in magnetic structure size distributions alone can explain the reduced brightness of regions with larger mean magnetic flux. This implies that, for the range of mean magnetic flux of the simulations, convective suppression plays at most a secondary role in determining radiative output of magnetized regions. Quantifying the role of convective transport over a wider range of mean magnetic flux is the subject of the second paper in this series.

Key words: Sun: activity – Sun: magnetic fields – Sun: photosphere

1. Introduction

Solar irradiance variations modulate important thermal and chemical processes in the Earth’s atmosphere, creating a need for models that reconstruct irradiance trends in the absence of accurate radiometric measurements (see, e.g., Gray et al. 2010; Ermolli et al. 2013; Coddington et al. 2016). Empirical models of the spectrally integrated total solar irradiance (TSI) can reproduce approximately 95% of the measured variability on solar cycle timescales by using proxy-measurements of the area covered by different magnetic structures on the solar disk (e.g., Lean 2010; Ball et al. 2012, 2014; Chapman et al. 2012). The agreement between TSI measurements and these models suggests that solar radiative variability is largely driven by varying solar surface coverage of magnetic structures (Chapman et al. 1996; Fligge et al. 1998; Unruh et al. 1999; Krivova et al. 2003; Ermolli et al. 2011; Yeo et al. 2017). However, some uncertainty exists in the ability of these models to reproduce observed spectral irradiance trends (see, e.g., Harder et al. 2009; Ermolli et al. 2013), which could suggest that current models may not properly account for the spectral irradiance of magnetic structures.

Given that the quiet Sun covers approximately 90% of the solar disk and contributes substantially to the total disk-integrated surface magnetic flux (e.g., Sánchez Almeida 2004; Domínguez Cerdeña et al. 2006), accurately quantifying the brightness contribution of the small-scale magnetic structures within the quiet Sun is critical for spectral irradiance modeling (Criscuoli et al. 2017). Assessing this observationally, however, is complicated by the difficulty in measuring quiet-Sun

brightness trends when using photometric measurements (Peck & Rast 2015) as regularly employed in irradiance models. From a theoretical perspective, the brightness of a small-scale magnetic structure, or flux tube, with respect to its surroundings results from balancing the effects of suppressed convection within the structure (due to the presence of the magnetic field) with enhanced lateral heating from the sidewalls (due to the reduced interior opacity; e.g., Spruit 1976; Spruit & Zwaan 1981; Deinzer et al. 1984; Criscuoli & Rast 2009). Structures with small radii appear bright compared to their surroundings due to greater efficiency of lateral radiative heating, while those with larger radii appear dark due to the suppressed convective heat transport and the relative inefficiency of the lateral heating. The transition from being brighter to darker than their surroundings occurs for structures with diameters of approximately 300–500 km (e.g., Knölker & Schüssler 1988; Keller 1992).

Some observations suggest that the brightness of magnetic structures may also depend on the mean magnetic flux of their extended surroundings. Studies evaluating the pixel-by-pixel brightness versus magnetogram signal have found a reduced brightness in active regions compared to quiet-Sun regions in both continuum (e.g., Title et al. 1992; Topka et al. 1992; Lawrence et al. 1993; Kobel et al. 2011, 2012; Criscuoli et al. 2017) and *G*-band observations (e.g., Romano et al. 2012). Using *Hinode* observations, Kobel et al. (2012) correlated a reduction in both contrast and line-of-sight velocity with increased surface magnetic flux averaged over the field of view. They concluded that a region with a larger mean magnetic flux

(i.e., an active region as opposed to a quiet-Sun region) acts to suppress the convective energy transport over the entire region, resulting in reduced heating and therefore darker magnetic structures compared to those in regions with lower mean magnetic flux. Criscuoli (2013) further studied this effect on small-scale magnetic structures using 3D MHD simulations characterized by different mean magnetic flux. They found that magnetic structures of roughly similar field strength and radius were darker when embedded in simulations with a larger mean magnetic flux, also attributing the effect to a reduction in convective energy transport.

The inferred role of suppressed convection on the brightness of magnetic structures embedded in regions with larger mean magnetic flux, however, could be influenced by low spatial resolution of both the observations and simulations. Low spatial resolution is known to significantly alter both the contrast and the inferred magnetic flux of small-scale magnetic structures (see, e.g., Title & Berger 1996; Criscuoli & Uitenbroek 2014), as well as the monotonic relationship between photospheric brightness and magnetic field strength (Röhrbein et al. 2011). Moreover, because the radiative output of magnetic structures is known to depend on their radius, the reduced brightness in active regions could instead result from larger, and therefore darker, magnetic structures underlying the resolution element of the observations. No studies to date have fully disentangled the role of differences in magnetic structure size distributions on the continuum brightness of regions of different mean magnetic flux from brightness changes in the region due to reduced convective transport.

In this work, we separately evaluate the role of magnetic structure size distributions and the effects of reduced convective transport in regions characterized by different mean magnetic flux using high-resolution 3D MHD simulations. The present paper addresses the former issue while a second will address the latter. Section 2 describes the simulations and analysis techniques used to evaluate magnetic structure sizes. In Section 3, we analyze the effect of the surface-averaged mean magnetic flux on the emergent intensity as a function of magnetic field strength, finding a reduction in brightness with increasing mean magnetic flux, in agreement with that found in previous studies. We then evaluate the differences in magnetic structure size distributions between the simulations, and demonstrate that the reduced brightness with increased mean magnetic flux can be explained by the differing magnetic structure size distributions. Finally, we compare the brightness of equal-sized magnetic structures embedded in regions with differing mean magnetic flux, and find no significant differences. In the Appendix, we argue that this difference from previous studies is likely due to the high spatial resolution of the simulations we employ.

In a second paper we will investigate the role of convective transport, particularly when the mean magnetic flux density of the examined region is higher. The results we present here suggest that, for magnetic flux densities in the range of what is typically called quiet Sun to active network (our simulations have unsigned magnetic flux densities in the range of 90–260 G), any contributions from changes in convective transport are secondary to those that result from changes in the magnetic structure size distributions.

2. Simulations and Analysis

This work utilizes 3D MHD simulations from the Max Planck Institute for Solar System Research/University of Chicago Radiation Magneto-hydrodynamics (MURaM) code (Vögler et al. 2005; Rempel et al. 2009). The simulations were computed on a grid with dimensions $6.144 \times 6.144 \times 3.072 \text{ Mm}^3$ and an 8 km grid spacing, with the modified bottom boundary condition discussed in Rempel (2014). We consider three simulations characterized by different mean magnetic flux, which we denote as the 0, 80, and 200 G simulations. The 0 G simulation was generated by introducing a randomly oriented seed field of 10^{-3} G into the thermally relaxed hydrodynamic simulation with no mean magnetic field imposed across the domain. The simulation was then evolved until the field amplitude saturated. The 0 G simulation closely matches observations of the small-scale dynamo magnetic field in Danilovic et al. (2010) and Danilovic et al. (2016), as well as observations of the Hanle depolarization in the Sr I 4607 Å line (del Pino Alemán et al. 2018). The 80 and 200 G simulations represent a magnetic morphology with a predominantly vertical magnetic field. These simulations were generated by introducing an 80 and 200 G vertical mean magnetic field, respectively, into the thermally relaxed hydrodynamic simulation, and again evolving until it reached steady state. For all three simulations, we evaluate 10 snapshots with a 4 minute cadence.

To compare the radiative output of the simulations, we synthesize the emergent intensity at $\lambda = 500$ nm for the vertical viewing angle—corresponding to disk center—using the RH radiative transfer solver (Uitenbroek 2001; Pereira & Uitenbroek 2015). For comparison with observational studies, we interpolate the grid-defined magnetic field vectors onto the $\tau_{500} = 1$ surface. Figure 1 shows the emergent intensity and vertical magnetic field at $\tau_{500} = 1$ for a single snapshot of the simulations. The average photospheric magnetic fields at $\tau_{500} = 1$ for the 10 snapshots of the three simulations are shown in Table 1. Note that the average unsigned magnetic flux $\langle |\mathbf{B}| \rangle$ for the 0 and 80 G simulations are roughly equivalent, saturating around 180 G, while the contribution from the horizontal and vertical components differ substantially. The 0 G simulation has, on average, a weaker vertical magnetic field and a stronger horizontal magnetic field than the 80 and 200 G simulations. The 0 and 80 G simulations therefore represent magnetic regions with equivalent unsigned magnetic flux, but differing magnetic morphologies.

To investigate the radiative properties of magnetic structures in the three simulations, we isolate them in the following way. First, we apply a mask to all simulation pixels with an unsigned vertical magnetic flux greater than 750 G at the $\tau_{500} = 1$ surface. This threshold was chosen based on the location of the minimum mean intensity in Figure 2, and represents the pixels where magnetic field has begun to concentrate in the downflow lanes to form magnetic structures (as inferred from the increase in mean intensity of pixels with B_z larger than 750 G; see Section 3 and Figure 2). Using this mask, we identify a magnetic structure as any collection of at least 50 pixels that are spatially adjoined.

According to the flux tube model (e.g., Spruit 1976; Spruit & Zwaan 1981; Deinzer et al. 1984), the brightness of a magnetic structure is related to the width of the tube, as well as the magnetic flux within the tube. In simulations and observations

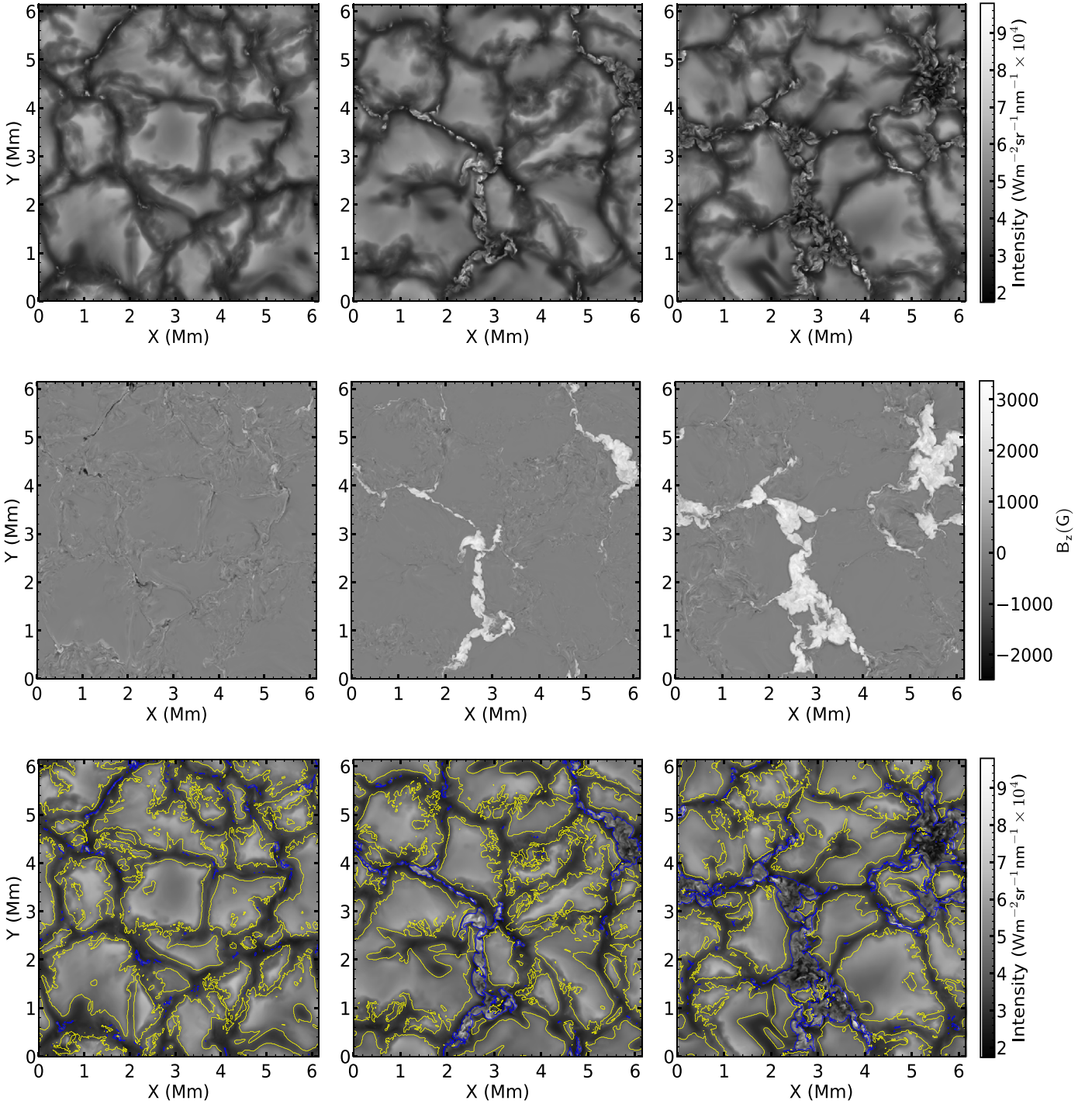


Figure 1. Top: emergent intensity at $\lambda = 500$ nm for a snapshot of the 0 G (left), 80 G (middle), and 200 G (right) simulations. Middle: vertical magnetic field, B_z , computed at the $\tau_{500} = 1$ surface. Bottom: intensity image with contours denoting magnetic structures (blue) and upflows (yellow). All remaining pixels were identified as downflow lanes.

Table 1

Average Unsigned Magnetic Field $\langle |B| \rangle$, Vertical Unsigned Magnetic Field $\langle |B_z| \rangle$, and Horizontal Magnetic Field $\langle |B_h| \rangle$ for the 10 Snapshots of the 0 G, 80 G, and 200 G Simulations

	$\langle B \rangle$	$\langle B_z \rangle$	$\langle B_h \rangle$
0 G	180 G	91 G	138 G
80 G	184 G	128 G	100 G
200 G	326 G	260 G	129 G

with limited spatial resolution, magnetic structures typically appear as flux tubes with a roughly circular cross-section, where the width of the tube is often estimated using the observed area of the cross-sectional circle. Given the high-resolution of the simulations used in this work, the cross-sections of the magnetic structures at the $\tau_{500} = 1$ surface range from circles to elongated sheets within the downflow lanes (see Figure 1). Since the horizontal heating of the sidewalls of magnetic structures is most efficient along the

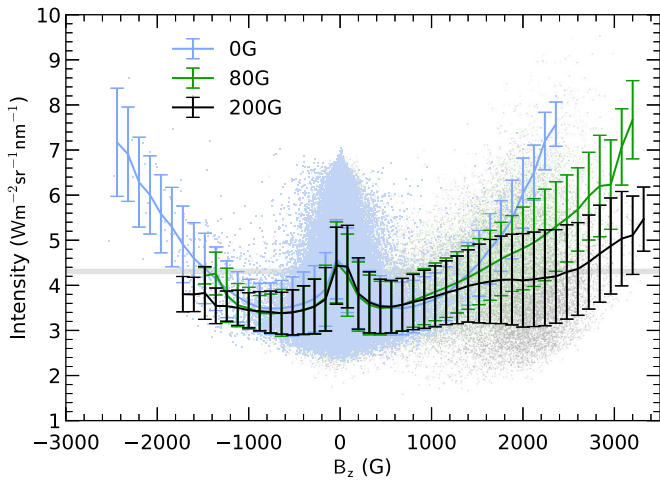


Figure 2. Disk-center emergent intensity at $\lambda = 500$ nm as a function of magnetic field. The average and standard deviation over equally spaced magnetic field bins is shown as solid lines. Horizontal gray band denotes the range of average intensity of the three simulations. Note the reduction in the average emergent intensity with increasing mean magnetic flux of the simulation, $\langle |B_z| \rangle$, for pixels with $B_z > 1200$ G.

smaller dimension of the magnetic structures, we utilize a fractal measurement that is heavily weighted toward this dimension. We define the fractal width (w) of a magnetic structure as the ratio of the area of the structure to its perimeter, where $w = \frac{4A}{P}$. The factor of 4 maintains equality of the measure with those for regular geometric structures (such as circles and squares). We compute the perimeter by applying a binary erosion algorithm (from the Scipy ndimage package Jones et al. 2001) to each identified structure. The algorithm removes all adjoined pixels on the border, so the number of pixels removed approximates the perimeter of the structure.

3. Results

We first directly compare the pixel-by-pixel emergent intensity and vertical magnetic field strength in the simulations to test if there exists a difference in the radiative output due to the mean magnetic flux of the region as found in previous works (Title et al. 1992; Lawrence et al. 1993; Kobel et al. 2011, 2012; Criscuoli 2013). Figure 2 shows scatterplots for the 10 snapshots in the three simulations, with the average and standard deviation over equally spaced 120 G magnetic field bins shown as solid lines. The horizontal gray band shows the range of the domain-averaged emergent intensity for all 10 snapshots of the three simulations. Pixels with $|B_z| \approx 0$ G are often found near the centers of granules, and are on average slightly brighter than the surroundings. Pixels with larger $|B_z|$ often correspond to regions in which the magnetic field begins to accumulate in the downflow lanes. For pixels with magnetic flux density larger than approximately $|B_z| = 750$ G, the average emergent intensity increases with increasing magnetic field strength. These typically correspond to pixels within magnetic structures.

Note that the 80 and 200 G simulations have no pixels with negative field greater than approximately -1500 G, while fields in the 0 G simulation extend to nearly -3000 G. This is a result of the mean vertical magnetic field in the 80 and 200 G simulations, which cancels a large fraction of the locally generated negative polarity field. In agreement with previous studies, the average emergent intensity for pixels with large B_z

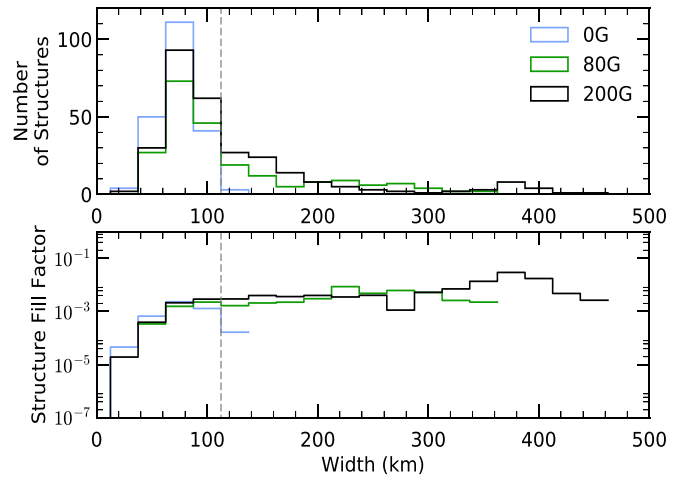


Figure 3. Top: histogram of all magnetic structures binned as a function of width. Bottom: fill factor of magnetic structures as a function of width. Note that despite fewer magnetic structures with large widths, the total area covered increases due to the large number of pixels comprising the largest magnetic structures. The vertical line roughly denotes the widest structure sizes present in all three simulations.

(greater than approximately 1200 G in our case) decreases with increasing mean magnetic flux of the simulation. The differences are as large as 50% at the highest magnetic field strengths. While these results agree with previous studies, our interpretation of the source of this reduction differs.

Inspection of Figure 1 suggests that the simulations have differing distributions of magnetic structure sizes. Given that the intensity differences in Figure 2 correspond to the high magnetic field pixels, which likely lie within the magnetic structures, we examine the distributions of magnetic structures as a function of their width. As shown in the top of Figure 3, the three simulations all have magnetic structures with widths up to around 115 km; however, unlike the 80 and 200 G simulations, the 0 G simulation has no structures larger than this. Furthermore, the largest magnetic structure width increases with increasing mean magnetic flux of the simulation. The lower panel in Figure 3 shows that despite a reduction in number of structures with widths larger than approximately 70 km, the integrated area of those structures increases. Wide structures consequently have a larger contribution to the radiative output trends than narrow structures.

We examine the role of magnetic structures in the observed trends in Figure 2 by removing magnetic structures wider than 115 km (the largest magnetic structure found in all three simulations) from the analysis, and replotting the pixel-by-pixel intensity versus B_z . As shown in Figure 4, this results in the same emergent intensity dependence in all three simulations. The reduction in the average intensity for large B_z in Figure 2 is therefore due to the presence of wide magnetic structures, which have both a larger integrated area and a lower radiative output than narrow magnetic structures (we elaborate on and illustrate this further below using Figure 5).

While the results in Figure 4 demonstrate that large magnetic structures are responsible for the observed reduction in emergent intensity with increasing mean magnetic flux, it does not rule out the possibility of differences in the brightness of equivalently sized magnetic structures due to differences in the mean magnetic flux of the extended region surrounding them. We therefore examine the radiative output of magnetic structures in the three simulations as a function of their width.

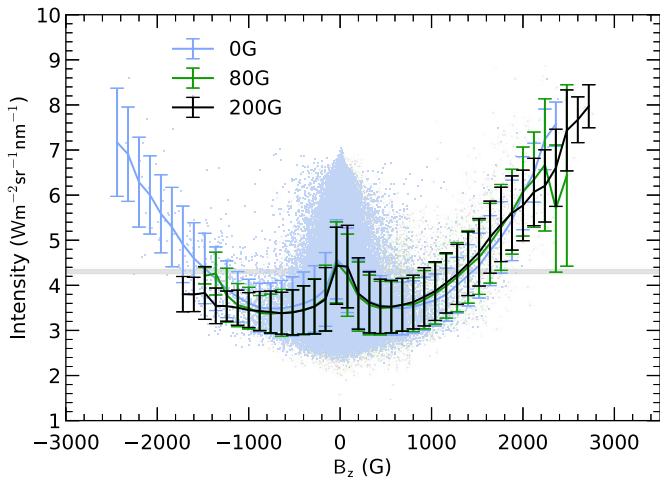


Figure 4. Same as Figure 2 excluding pixels corresponding to magnetic structures wider than 115 km. Note that removing these magnetic structures results in agreement between the three simulations compared to Figure 2.

The average magnetic structure intensity and vertical magnetic field as a function of width is shown in Figure 5(a). Note that the intensity of narrow magnetic structures in all simulations increases with increasing width, which also corresponds to an increase in the magnetic flux of the element (indicated by the symbol color in Figure 5). Beyond a width of about 160 km, however, the average intensity of the structure decreases while its average magnetic flux continues to increase. This is not a result of using the fractal definition for the magnetic structure width. As shown in Figure 5(b), we find qualitatively similar results using the equivalent radius (approximating the cross-section of the structure as a circle, as employed in previous work), though the curve seems less well defined for this more common measure of size.

As stated previously, the turnover from increasing to decreasing intensity as a function of width occurs at roughly 160 km. This coincides with the value of the average width of the downflow lanes calculated using the same area and perimeter scheme as used for the magnetic structures. This suggests that once the width of the magnetic structures is roughly equivalent to the downflow lane width, the presence of the magnetic field begins to reduce the convective efficiency locally within the magnetic structure, resulting in reduced heating and therefore darkening of the structure. This is qualitatively consistent with the flux tube model predictions. Most importantly, the relationships between size and intensity are statistically equivalent in the three simulations despite the differences in mean magnetic flux densities.

4. Discussion and Conclusions

In this work, we used high-spatial resolution 3D MHD simulations to evaluate the role of changes in the magnetic structure size distribution on the observed reduction in continuum brightness with increasing mean magnetic flux of an extended solar surface region. We employed three high-resolution simulations characterized by differing mean magnetic flux on an optical depth surface. The 0 G simulation has a large horizontal component of the magnetic field, representing a magnetic field configuration produced by a small-scale dynamo, while the 80 and 200 G simulations represent regions with a predominantly vertical magnetic field with differing mean magnetic flux. We synthesized the emergent intensity in

the simulations at $\lambda = 500$ nm for the vertical line of sight and computed the magnetic field at the $\tau_{500} = 1$ surface.

A pixel-by-pixel analysis of the emergent intensity as a function of the vertical magnetic field strength in the three simulations (Figure 2) reveals lower intensities at strong magnetic field locations in simulations with larger mean magnetic flux. This agrees with results from previous studies (e.g., Title et al. 1992; Topka et al. 1992; Lawrence et al. 1993; Kobel et al. 2011, 2012; Criscuoli 2013; Criscuoli et al. 2017). For the simulations used in this work, this difference is due to the differing magnetic structure morphologies to which the strong-field pixels belong. Wider structures are found in simulations with a larger mean magnetic flux than those with lower mean flux (Figure 3). After removing the contribution of magnetic structures wider than around 115 km (the widest structure found in all three simulations), the pixel-by-pixel analysis yielded intensity-magnetic field relations that no longer differed between the simulations for strong magnetic field values. Moreover, the radiative output of magnetic structures of equivalent width is the same for all simulations, independent of the value of the mean field (Figure 5(a)). There are no statistically significant differences between the brightness of equal-sized magnetic structures in the three simulations. The only difference between them is the number of structures of a given size, with wider structures found more often in simulations with larger mean field.

We compare our results with those found by Criscuoli (2013), who also studied the brightness of small-scale magnetic structures in simulations characterized by different mean magnetic field strength. They concluded that magnetic structures embedded in regions of higher mean magnetic flux had reduced brightness compared to those in regions of lower mean magnetic flux (their Table 1). They also measured the velocities inside and outside the magnetic structures, and attributed the reduced brightness to reduced convective efficiency. A number of differences exist between the studies. Evaluation of their Table 1 shows a relatively coarse binning in size and differences in brightness that are small (lie within one standard deviation). In the Appendix we show that when duplicating their analysis using more data and finer radius bins, we achieve results inline with those found in this work—equivalent brightness–size relationships for the magnetic structures despite differences in the mean magnetic flux and convective efficiency. Moreover, the simulations used in Criscuoli (2013) were of significantly lower resolution. In the Appendix we also make an assessment of the impact of this, showing reduced brightness–size trends at the resolution of the previous studies. Similar resolution and binning effects may have also impacted previous observational studies. For example, in contrast to findings by Romano et al. (2012), recent results by Liu et al. (2018) indicate that the brightness–size relation for *G*-band bright points does not depend on the magnetic flux density of the surrounding plasma.

More generally, because of observational limitations, many previous studies (e.g., Title et al. 1992; Topka et al. 1992; Lawrence et al. 1993; Kobel et al. 2011, 2012; Criscuoli et al. 2017) evaluated magnetic structures much larger than those considered here. While our work focused on small-scale magnetic structures, the results suggest that correct interpretation of the pixel-by-pixel intensity as a function of line-of-sight magnetic field strength also requires an understanding of the magnetic structure size distributions. This is particularly

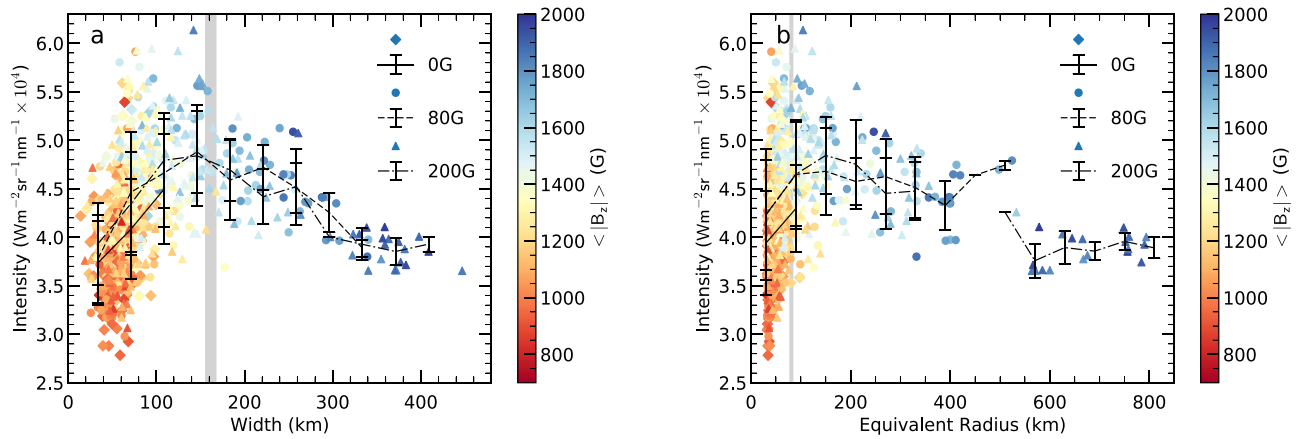


Figure 5. Average intensity of magnetic structures as a function of width (a) and equivalent radius (b). The color bar denotes the magnetic flux of the structure (average magnetic field of the element at the $\tau_{500} = 1$ surface). The vertical gray band represents the range of average downflow lane widths in the three simulations. Note that the downturn of the intensity corresponds roughly to the width of downflow lanes.

difficult for unresolved magnetic structures, even when some assessment of the subpixel filling factor is made (e.g., Kobel et al. 2011, 2012).

We note that this work has not included an assessment of convective transport. Suppression of convective transport may well play a more important role in regions of stronger field and/or larger magnetic flux structures, such as those found in the studies of Kobel et al. (2011, 2012). Quantifying this effect requires going well beyond measuring convective velocities in and around magnetic structures, as it is delicate correlations between enthalpy fluctuations and the plasma velocity that determine the convective flux. Moreover, kinetic energy transport must be accounted for in both the magnetic structures and the surrounding plasma. These balances, their relationship to the radiative environment of magnetic structures, and the consequent importance of convective suppression as a function of mean magnetic field strength will be the subject of a follow-up study.

Finally, we note that while current observations face difficulties in evaluating the brightness–size relation of small-scale magnetic structures, upcoming high-resolution observations from NSF’s 4 m Daniel K. Inouye Solar Telescope (DKIST, Elmore et al. 2014; Tritschler et al. 2016) and the upcoming 4 m European Solar Telescope (Collados et al. 2013; Matthews et al. 2016) will allow us to probe the brightness–size relations of various magnetic regions in detail. Next generation high-resolution observations will likely reveal complex magnetic structures, perhaps similar to those seen in our simulations. These, in general, do not resemble flux tubes with circular cross-sections. Given the improvement in the plot of magnetic structure brightness versus flux element width (Figure 5), we suggest the fractal width measurement proposed here for use in future high-resolution studies rather than the more commonly employed effective radius.

This material is based upon work partially supported by the National Science Foundation under grant No. 1616538. The National Solar Observatory is operated by the Association of Universities for Research in Astronomy under a cooperative agreement with the National Science Foundation. The National Center for Atmospheric Research is sponsored by the National Science Foundation. This work utilized the RMACC Summit supercomputer, which is supported by the National Science Foundation (awards ACI-1532235 and ACI-1532236), the

University of Colorado Boulder, and Colorado State University. The Summit supercomputer is a joint effort of the University of Colorado Boulder and Colorado State University. The authors are grateful for the International Space Science Institute in Bern for hosting the International Team 335 “Toward New Models of Solar Spectral Irradiance Based on 3D MHD Simulations,” which helped motivate this work.

Software: MURaM (Vögler et al. 2005; Rempel et al. 2009), RH (Uitenbroek 2001; Pereira & Uitenbroek 2015), Stagger (Nordlund & Galsgaard 1995), Scipy ndimage (Jones et al. 2001).

Appendix

We utilize 50 simulation snapshots for three simulation sets (for a total of 150 snapshots) with different mean vertical magnetic field strengths employed in Criscuoli (2013) to compare the radiative behavior of magnetic structure trends in their simulations with the results from this work. These simulations were calculated with the Stagger code (Nordlund & Galsgaard 1995) with a grid spacing of 24 km per pixel in the horizontal direction. The simulations have been used in a variety of studies, described in detail in Fabbian et al. (2010), Criscuoli (2013), and Criscuoli & Foukal (2017). The Stagger simulations represent three regions characterized by mean magnetic fluxes of 50, 100, and 200 G. We employ the magnetic structure identification scheme used in this work to isolate the magnetic structures. Figure 6(a) shows the magnetic structure intensity as a function of the equivalent radius. In agreement with results from this work, there is no statistically significant difference between the radiative output of the magnetic structures for simulations with differing mean magnetic field.

Note that the brightness trend as a function of equivalent radius in Figure 6(a) lies within the standard deviation of the structure intensities, and that the amplitude of the trend is greatly reduced compared to Figure 5(b). We demonstrate that this reduction in the trend can be attributed to the lower spatial resolution of the Stagger simulations compared with the MURaM simulations used in this work. We approximate the lower resolution of the Stagger simulations by smoothing the emergent intensity and magnetic field of the MURaM simulations with a convolution kernel to match the Stagger resolution, and downsample the smoothed images to match the

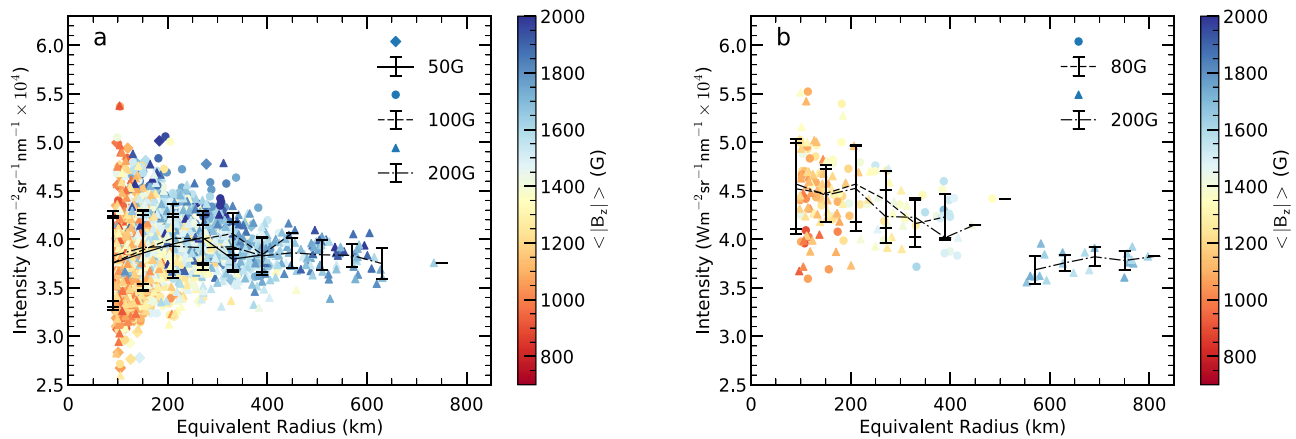


Figure 6. (a) Average intensity of magnetic structures as a function of equivalent radius for the Stagger simulations used in Criscuoli (2013) and (b) for simulations used in this work smoothed and downsampled to approximately match the reduced resolution of the Stagger simulations. The color bar denotes the magnetic flux of the structure (average magnetic field of the element at the $\tau_{500} = 1$ surface).

Stagger grid sampling. Figure 6(b) shows the results obtained by applying the same magnetic structure identification scheme used throughout this work to the smoothed, downsampled MURaM intensity and magnetic field images. Note that the trend qualitatively matches those found in Figure 6(a). The effect of smoothing the intensity and magnetic field of the MURaM simulations results in a reduced magnetic structure intensity trend compared to the trend found for high-resolution simulations (Figure 5(b)).

ORCID iDs

C. L. Peck <https://orcid.org/0000-0002-7586-4220>
M. P. Rast <https://orcid.org/0000-0002-9232-9078>
S. Criscuoli <https://orcid.org/0000-0002-4525-9038>
M. Rempel <https://orcid.org/0000-0001-5850-3119>

References

- Ball, W. T., Krivova, N. A., Unruh, Y. C., Haigh, J. D., & Solanki, S. K. 2014, *JAtS*, **71**, 4086
- Ball, W. T., Unruh, Y. C., Krivova, N. A., et al. 2012, *A&A*, **541**, A27
- Chapman, G. A., Cookson, A. M., & Dobias, J. J. 1996, *JGR*, **101**, 13541
- Chapman, G. A., Cookson, A. M., & Preminger, D. G. 2012, *SoPh*, **276**, 35
- Coddington, O., Lean, J. L., Pilewskie, P., Snow, M., & Lindholm, D. 2016, *BAMS*, **97**, 1265
- Collados, M., Bettonvil, F., Cavaller, L., et al. 2013, *MmSAI*, **84**, 379
- Criscuoli, S. 2013, *ApJ*, **778**, 27
- Criscuoli, S., & Foukal, P. 2017, *ApJ*, **835**, 99
- Criscuoli, S., Norton, A., & Whitney, T. 2017, *ApJ*, **847**, 93
- Criscuoli, S., & Rast, M. P. 2009, *A&A*, **495**, 621
- Criscuoli, S., & Uitenbroek, H. 2014, *A&A*, **562**, L1
- Danilovic, S., Rempel, M., van Noort, M., & Cameron, R. 2016, *A&A*, **594**, A103
- Danilovic, S., Schüssler, M., & Solanki, S. K. 2010, *A&A*, **513**, A1
- Deinzer, W., Hensler, G., Schüssler, M., & Weisshaar, E. 1984, *A&A*, **139**, 426
- del Pino Alemán, T., Trujillo Bueno, J., Štěpán, J., & Shchukina, N. 2018, *ApJ*, **863**, 164
- Domínguez Cerdeña, I., Sánchez Almeida, J., & Kneer, F. 2006, *ApJ*, **636**, 496
- Elmore, D. F., Rimmele, T., Casini, R., et al. 2014, *Proc. SPIE*, 9147, 914707
- Ermolli, I., Criscuoli, S., & Giorgi, F. 2011, *CoSKL*, **41**, 73
- Ermolli, I., Matthes, K., Dudok de Wit, T., et al. 2013, *ACP*, **13**, 3945
- Fabbian, D., Komenko, E., Moreno-Insertis, F., & Nordlund, Å. 2010, *ApJ*, **724**, 1536
- Fligge, M., Solanki, S. K., Unruh, Y. C., Fröhlich, C., & Wehrli, C. 1998, *A&A*, **335**, 709
- Gray, L. J., Beer, J., Geller, M., et al. 2010, *RvGeo*, **48**, RG4001
- Harder, J. W., Fontenla, J. M., Pilewskie, P., Richard, E. C., & Woods, T. N. 2009, *GeoRL*, **36**, L07801
- Jones, E., Oliphant, T., Peterson, P., et al. 2001, SciPy: Open Source Scientific Tools for Python, <http://www.scipy.org/>
- Keller, C. U. 1992, *Natur*, **359**, 307
- Knölker, M., & Schüssler, M. 1988, *A&A*, **202**, 275
- Kobel, P., Solanki, S. K., & Borrero, J. M. 2011, *A&A*, **531**, A112
- Kobel, P., Solanki, S. K., & Borrero, J. M. 2012, *A&A*, **542**, A96
- Krivova, N. A., Solanki, S. K., Fligge, M., & Unruh, Y. C. 2003, *A&A*, **399**, L1
- Lawrence, J. K., Topka, K. P., & Jones, H. P. 1993, *JGR*, **98**, 18
- Lean, J. L. 2010, *Wiley Interdisciplinary Reviews: Climate Change*, **1**, 111
- Liu, Y., Xiang, Y., Erdélyi, R., et al. 2018, *ApJ*, **856**, 17
- Mathews, S. A., Collados, M., Mathioudakis, M., & Erdélyi, R. 2016, *Proc. SPIE*, 9908, 990809
- Nordlund, Å., & Galsgaard, K. 1995, A 3D MHD code for Parallel Computers, Tech. Rep., Astron. Observ., Copenhagen University, https://www.astro.ku.dk/~kg/Papers/MHD_code.ps.gz
- Peck, C. L., & Rast, M. P. 2015, *ApJ*, **808**, 192
- Pereira, T. M. D., & Uitenbroek, H. 2015, *A&A*, **574**, A3
- Rempel, M. 2014, *ApJ*, **789**, 132
- Rempel, M., Schüssler, M., & Knölker, M. 2009, *ApJ*, **691**, 640
- Röhrbein, D., Cameron, R., & Schüssler, M. 2011, *A&A*, **532**, A140
- Romano, P., Berrilli, F., Criscuoli, S., et al. 2012, *SoPh*, **280**, 407
- Sánchez Almeida, J. 2004, in ASP Conf. Ser. 325, *The Solar-B Mission and the Forefront of Solar Physics*, ed. T. Sakurai & T. Sekii (San Francisco, CA: ASP), 115
- Spruit, H. C. 1976, *SoPh*, **50**, 269
- Spruit, H. C., & Zwaan, C. 1981, *SoPh*, **70**, 207
- Title, A. M., & Berger, T. E. 1996, *ApJ*, **463**, 797
- Title, A. M., Topka, K. P., Tarbell, T. D., et al. 1992, *ApJ*, **393**, 782
- Topka, K. P., Tarbell, T. D., & Title, A. M. 1992, *ApJ*, **396**, 351
- Tritschler, A., Rimmele, T. R., Berukoff, S., et al. 2016, *AN*, **337**, 1064
- Uitenbroek, H. 2001, *ApJ*, **557**, 389
- Unruh, Y. C., Solanki, S. K., & Fligge, M. 1999, *A&A*, **345**, 635
- Vögler, A., Shelyag, S., Schüssler, M., et al. 2005, *A&A*, **429**, 335
- Yeo, K. L., Solanki, S. K., Norris, C. M., et al. 2017, *PhRvL*, **119**, 9